Revision 1

Word Count: 6636

Heamanite-(Ce), $(K_{0.5}Ce_{0.5})TiO_3$, a new perovskite supergroup mineral found in diamond from Gahcho Kué, Canada

Chiara Anzolini[1,*], William K. Siva-Jothy[1], Andrew J. Locock[1], Fabrizio Nestola[2], Tonči Balić-Žunić[3], Matteo Alvaro[4], Ingrid L. Chinn[5], Thomas Stachel[1], D. Graham Pearson[1]

[1]Department of Earth and Atmospheric Sciences, 1-26 Earth Sciences Building, University of Alberta, Edmonton, Alberta T6G 2E3, Canada

[2]Department of Geosciences, University of Padova, Via G. Gradenigo 6, 35131 Padova, Italy

[3]Department of Geosciences and Natural Resource Management, University of Copenhagen, Øster Voldgade 10, 1350 Copenhagen, Denmark

[4]Department of Earth and Environmental Sciences, University of Pavia, Via A. Ferrata 1, 27100 Pavia, Italy

[5]De Beers Group Services (Pty) Ltd, Private Bag X01, Southdale, 2193 Johannesburg, South Africa

*Corresponding author: Chiara Anzolini (anzolini@ualberta.ca)

Abstract

Heamanite-(Ce) (IMA 2020-001), ideally $(K_{0.5}Ce_{0.5})TiO_3$, is a new perovskite-group mineral found as an inclusion in a diamond from the Gahcho Kué mine in the Northwest Territories, Canada. It occurs as brown, translucent single crystals with average maximum dimension of ~80 μm, associated with rutile and calcite. The luster is adamantine and the fracture conchoidal. Heamanite-(Ce) is the K-analog of loparite-(Ce), ideally $(NaCe)Ti_2O_6$. The Mohs hardness is estimated to be 5½ by comparison to loparite-(Ce) and the calculated density is 4.73(1) g/cm^3. Electron microprobe wavelength-dispersive spectrometric analysis (average of 34 points) yielded: CaO 10.70, K_2O 7.38, Na_2O 0.16, Ce_2O_3 13.77, La_2O_3 8.22, Pr_2O_3 0.84, Nd_2O_3 1.59, SrO 6.69, BaO 2.96, ThO_2 0.36, PbO 0.15, TiO_2 45.77, Cr_2O_3 0.32, Al_2O_3 0.10, Fe_2O_3 0.09, Nb_2O_5 0.87, UO_3 0.01, total 99.98 wt.%. The empirical formula, based on 3 O atoms, is: $[(K_{0.268}Na_{0.009})_{\Sigma 0.277}(Ce_{0.143}La_{0.086}Pr_{0.009}Nd_{0.016})_{\Sigma 0.254}(Ca_{0.326}Sr_{0.110}Ba_{0.033}Pb_{0.001})_{\Sigma 0.470}Th_{0.002}]_{\Sigma 1.003}($ $Ti_{0.979}Nb_{0.011}Cr_{0.007}Al_{0.003}Fe_{0.002})_{\Sigma 1.002}O_3$. The Goldschmidt tolerance factor for this formula is 1.003. Heamanite-(Ce) is cubic, space group $Pm\bar{3}m$, with unit-cell parameter a = 3.9129(9) Å, and volume V = 59.91(4) Å^3 (Z = 1). The crystal structure was solved using single-crystal X-ray diffraction data and refined to $R_1(F)$ = 2.61%. Heamanite-(Ce) has the aristotypic perovskite structure and adopts the same structure as isolueshite and tausonite. The six strongest diffraction lines are [d_{obs} in Å (I in %) (h k l)]: 2.764 (100) (1 1 0) , 1.954 (41) (2 0 0), 1.596 (36) (2 1 1), 1.045 (16) (3 2 1), 1.236 (13) (3 1 0) and 1.382 (10) (2 2 0). The Raman spectrum of heamanite-(Ce) shows two broad bands at 560 and 787 cm^{-1}, with no bands observed above 1000 cm^{-1}. Heamanite-(Ce) is named after Larry Heaman, a renowned scientist in the field of radiometric dating applied to diamond-bearing kimberlites, mantle-derived eclogites, and lamprophyre dikes. The dominant REE should appear as a Levinson suffix, hence heamanite-(Ce).

Keywords: Heamanite-(Ce), new mineral, perovskite, crystal structure, loparite-(Ce), diamond inclusion, mantle, Gahcho Kué.

Introduction

Diamonds, thanks to their particular properties, are the only carriers able to sample pieces of the upper mantle (see Stachel and Harris 2008 for an extensive review), the transition zone (Moore and Gurney 1985; Deines et al. 1991; Pearson et al. 2014; Kiseeva et al. 2016; Tschauner et al. 2018) and even the lower mantle (Scott Smith et al. 1984; Harte et al. 1999; Stachel et al. 2000; Smith et al. 2016; Smith et al. 2018; Nestola et al. 2018), and protect them during transport up to the surface via kimberlites and lamproites. Indeed, their extreme strength and refractory nature not only permit diamonds to survive exhumation to the Earth's surface and any subsequent weathering, but also to act as a shield to protect any mineral and fluid inclusions that they carry. Even if other mantle materials, such as mantle xenoliths and exposed mantle rocks, are directly observable, the deeper into the earth that we want to sample, the more we have to rely upon diamond to provide material for study. For this reason, the investigation of diamonds and their inclusions has allowed the discovery of the natural occurrences of high-pressure phases previously known only from experimental studies (Harte et al. 1999; Stachel et al. 2000; McCammon 2001; Brenker et al. 2002; Harte and Hudson 2013; Pearson et al. 2014; Anzolini et al. 2016; Nestola et al. 2018), and also has led to the new mineral species: jeffbenite ($Mg_3Al_2Si_3O_{12}$, previously known as TAPP, Nestola et al. 2016), ice-VII (H_2O, Tschauner et al. 2018), goldschmidtite [$(K,REE,Sr)(Nb,Cr)O_3$, Meyer et al. 2019] and breyite ($CaSiO_3$ with the walstromite structure-type, Brenker et al. 2021).

In this paper we present heamanite-(Ce), the first natural occurrence of $(K_{0.5}Ce_{0.5})TiO_3$ found within a diamond from the Gahcho Kué mine, Northwest Territories, Canada (Fig. 1). Heamanite-(Ce) represents the K-analog of loparite-(Ce), whose ideal composition is $(NaCe)Ti_2O_6$. It is the sixth perovskite-structured mineral to occur in Earth's mantle, along with perovskite *sensu stricto* ($CaTiO_3$), K-REE-Cr-rich tausonite (Kopylova et al. 1997a,b), bridgmanite [$(Mg,Fe)SiO_3$, Harte et al. 1999; Tschauner et al. 2014], $CaSiO_3$-perovskite (Nestola et al. 2018), and goldschmidtite [$(K,REE,Sr)(Nb,Cr)O_3$, Meyer et al. 2019]. We describe the physical, chemical, optical and structural properties of the new mineral heamanite-(Ce) and suggest a possible mechanism of formation. Heamanite-(Ce) is named after Larry Heaman (b. 1955), who is a Distinguished University Professor at the University of Alberta in Edmonton, Canada. Larry Heaman's highly recognized research aims to elucidate the evolution of Earth's crust and mantle through time with the help of radiogenic isotope systems (U-Pb, Rb-Sr, Sm-Nd, Lu-Hf). In particular, he has had a prolific career determining the age of diamond-bearing kimberlites, mantle-derived eclogites, and lamprophyre dikes from around the world. Larry Heaman's research has been instrumental in establishing baddeleyite (ZrO_2) and perovskite as key minerals for high-precision U-Pb dating of mafic igneous rocks. His internationally acclaimed work on establishing emplacement ages for ultramafic dike swarms has been critical for the reconstruction of Precambrian super-continent configurations (Heaman 1997). Larry Heaman's high precision dating of kimberlite emplacement ages allowed him, for the first time, to link kimberlite activity to the trace of a hot spot, in this case the passage of the Great Meteor hot spot beneath Eastern North America (Heaman and Kjarsgaard 2000). Through his dating work, Larry Heaman has provided a critical service to the diamond exploration industry in North America since the early 1990s.

Following the IMA−CNMNC dominant-valency rule (Bosi et al. 2019), both K and REE are essential constituents in the new mineral described herein. Therefore, the role of the dominant REE is crucial, and the dominant REE should appear as a suffix (Levinson 1966), hence heamanite-(Ce). Heamanite-(Ce) has been approved by the Commission on New Minerals, Nomenclature and Classification with the code IMA 2020-001, and the holotype material is deposited at the Royal Ontario Museum (Canada), under catalog number M59970.

Experimental methods

Electron probe microanalysis

Six heamanite-(Ce) inclusions (Fig. 2) were released by crushing the diamond in a steel diamond cracker. The released mineral grains were mounted in epoxy, roughly ground with corundum paper and then polished with 1 μm diamond suspension on a nylon cloth. Heamanite-(Ce) was analyzed by electron probe microanalysis (EPMA) on a CAMECA SX100 at the Department of Earth and Atmospheric Sciences, University of Alberta. The analyses were conducted using wavelength dispersive spectrometry (WDS) and an accelerating voltage of 20 kV, probe current of 20 nA, and a fully focused beam (< 1 μm) for the 18 oxides CaO, K_2O, Na_2O, Ce_2O_3, La_2O_3, Pr_2O_3, Nd_2O_3, SrO, BaO, ThO_2, PbO, TiO_2, Cr_2O_3, Al_2O_3, Fe_2O_3, Nb_2O_5, UO_3 and MgO. The precision for the major elements is better than 1%. Limits of detection were calculated in the Probe for EPMA software (Donovan et al. 2015) at the 99% confidence limit to be (in parts per million, rounded to the nearest 10 ppm): Ca 90, K 90, Na 130, Ce 340, La 310, Pr 330, Nd 330, Sr 380, Ba 330, Th 520, Pb 370, Ti 130, Cr 120, Al 70, Fe 100, Nb 380, U 280, Mg 90. Mg was not found at concentrations above the detection limit. Oxide abundances and the

standards used are listed in Table 1. The proportions of the perovskite-charge-arrangement components were calculated by using the Excel spreadsheet of Locock and Mitchell (2018) and are (standard deviations in parentheses): 51.37 (0.36)% heamanite/loparite ($(K,Na)_{0.5}REE_{0.5}TiO_3$), 32.90 (0.35)% perovskite ($CaTiO_3$), 11.14 (0.16)% tausonite ($SrTiO_3$), 3.33 (0.04)% barioperovskite ($BaTiO_3$), and 1.13 (0.05)% lueshite ($NaNbO_3$). The heamanite-(Ce) composition is plotted on the tausonite – perovskite – loparite & heamanite and $[(Na,K)NbO_3]$ – $[(Ca,Sr,Ba,Pb)TiO_3]$ – $[(Na,K)_{0.5}REE_{0.5}TiO_3]$ ternary diagrams (Fig. 3).

Single-crystal X-ray diffraction

One heamanite-(Ce) crystal (87A; Fig. 2a) was extracted from a polished mount under a reflected light microscope and attached to a glass fiber (Fig. 4). X-ray diffraction data were collected using a Rigaku Oxford Diffraction XtaLAB SuperNova single-crystal diffractometer (kappa-geometry), equipped with a Dectris Pilatus3 R 200K-A area detector and a Mova X-ray micro-source (beam spot of 120 μm), at the Department of Earth and Environmental Sciences, University of Pavia. Monochromatized Mo *K*α radiation (λ = 0.71073 Å), working t 50 kV and 0.8 mA, was used. The sample-to-detector distance was 68 mm. Intensity data used to produce a crystallographic information file (CIF) were collected up to $2\theta_{max}$ = 98.90° over 14 runs and 1368 frames (redundancy = 42.8) with an exposure time of 40 s per frame and a total measurement time of about 15 h.

Micro-Raman spectroscopy

The same crystal subsequently investigated by single-crystal X-ray diffraction (87A, Fig. 4) was first analyzed by micro-Raman spectroscopy. Raman measurements were carried out

at the Nanotechnology Research Centre (National Research Council), University of Alberta, using a Thermo Scientific DXR2 Raman Microscope with a grating of 1800 grooves per mm in the optical path. A 532 nm laser was used at a power of 8 mW; spectra were collected for 10 s, averaged over 24 accumulations for a total of 4 min per spectrum. The analysis was performed using a 50× objective with a spatial resolution of 1.1 μm and a spectral resolution estimated to be ~1.6–2.0 cm^{-1}. Data were collected between 50 and 1875 cm^{-1}.

Results

Appearance, physical and optical properties

Heamanite-(Ce) occurs as single discrete crystals, with average maximum dimension of ~80 μm (Fig. 2), whose habit was probably imposed by the diamond host. The mineral is brown, translucent and has an adamantine luster. The limited thickness of the grains prevented the determination of streak, cleavage, parting, tenacity and fracture properties. However, we can assume the cleavage and tenacity to be similar to those of its Na-analog, loparite-(Ce), which is brittle and cleaves along the {100} form. Although the fracture was not observed in the free-standing grains, it is probably conchoidal based on observations of the polished grains (Fig. 2).

Although the density of heamanite-(Ce) was not measured because of the small size of the mineral grains, the density was calculated to be 4.73(1) g/cm^3, based on the unit-cell volume determined by X-ray diffraction and the chemical composition determined by electron probe microanalysis. The hardness was not determined because of the small size and brittleness of the material available. However, heamanite-(Ce) is the K-analog of loparite-(Ce), ideally $(Na,Ce)Ti_2O_6$, which has hardness 5½ on the Mohs scale. As natural loparite-(Ce) has a density between 4.75 and 4.94 g/cm^3 and heamanite-(Ce) has a calculated density of 4.73(1) g/cm^3, it is

reasonable to expect that they have similar hardness. Attempts were made to measure the Vickers microhardness of heamanite-(Ce); despite trying different loads, however, the crystal cracked because of its limited thickness (Supplemental Fig. S1). Therefore, in order to preclude further destructive measurements, and to maximize the amount of archived material, the attempts to measure micro-hardness were not continued.

The refractive index of heamanite-(Ce) was computed using the Gladstone-Dale constants of Mandarino (1976) the chemical composition and the calculated density to be $n_{calc} = 2.28$, which is the same as the calculated average refractive index of loparite-(Ce).

Chemical composition

The empirical formula of heamanite-(Ce) calculated from the EPMA data in Table 1, on the basis of 3 oxygens atoms per formula unit (apfu) is: $[(K_{0.268}Na_{0.009})_{\Sigma 0.277}(Ce_{0.143}La_{0.086}Pr_{0.009}Nd_{0.016})_{\Sigma 0.254}(Ca_{0.326}Sr_{0.110}Ba_{0.033}Pb_{0.001})_{\Sigma 0.470}Th_{0.002}]_{\Sigma 1.003}(Ti_{0.979}Nb_{0.011}Cr_{0.007}Al_{0.003}Fe_{0.002})_{\Sigma 1.002}O_3$. The Goldschmidt tolerance factor for this formula is 1.003, which is consistent with cubic symmetry. The simplified formula is $[\{(K,Na)(Ce,La)\},(Ca,Sr)](Ti,Nb)O_3$ and the ideal formula is $(K_{0.5}Ce_{0.5})TiO_3$, which requires K_2O 12.70, Ce_2O_3 44.24, TiO_2 43.06 for a total of 100 wt.%.

X-ray crystallography

Data reduction of the single-crystal X-ray diffraction intensities was performed using the CrysAlisPro software (Rigaku Oxford Diffraction; https://www.rigaku.com/en/products/smc/crysalis). The data were corrected for Lorentz and polarization effects, and the absorption correction was performed by running the interframe scaling implemented in CrysAlisPro, resulting in a final $R_{int} = 2.31\%$. As both the chemical

composition (Goldschmidt tolerance factor of 1.003) and the X-ray intensities are consistent with cubic symmetry, the unit cell dimension was refined in the cubic system using 1132 reflections. The refined unit-cell parameter is a = 3.9129(9) Å, and volume is V = 59.91(4) Å^3 (Z = 1).

Powder X-ray diffraction data were not determined experimentally due to the very small amount of material available; a powder diffraction pattern calculated from the single-crystal measurements is given in Table 2, where a comparison between observed and calculated data are reported (the calculated data were obtained using Vesta software and the structure data, Momma and Izumi 2011). Using the observed *d*-spacing reported in Table 2 and the software UnitCell (Holland and Redfern 1997), we obtained the following unit-cell dimensions: a = 3.9099(2) Å, and V = 59.771(7) Å^3 (Z = 1). The peaks at 3.035 and 2.089 Å, which could not be indexed with the unit cell of heamanite-(Ce), were identified as resulting from the presence of a minor amount of calcite. A comparison of heamanite-(Ce) with the other natural cubic perovskites that have alkali-metals and Ti or Nb is given in Supplemental Table S1.

Crystal structure

The crystal structure was solved with the software suite JANA2006 (Petříček et al. 2014). The structure-solving program Superflip, which is a part of JANA2006, indicated cubic symmetry with space group $Pm\bar{3}m$. Attempts to solve and refine the structure in the lower symmetry space groups *I*4/*mcm* (No. 140) and *Pnma* (No. 62) did not yield suitable results. Preliminary refinement in $Pm\bar{3}m$ yielded a perovskite-related structural model, ABO_3, with highly anisotropic atomic displacement parameters for the oxygen atom in the form of an oblate rotational ellipsoid with the rotation axis oriented towards the *B* site.

The anisotropy of the atomic displacement parameter indicated that the oxygen site should be modelled as a split site. There are two simple ways to split the oxygen site in accordance with the described anisotropic atomic displacement parameter: to displace it to a site 12*h* (*x*, 0, ½) or to 12*i* (*x*, 0, *x*). A calculated F_o Fourier map around the oxygen site (Fig. S2) is consistent with the former mode of splitting, which also gave slightly better *R* factors. Identical splitting of the oxygen position in the isostructural mineral isolueshite, $NaNbO_3$, was reported by Krivovichev et al. (2000). The final refinement was carried out using SHELXL software (Sheldrick 2015) in the WinGX package (Farrugia 2012). The isotropic refinement gave an agreement factor $R_1 = 2.61\%$ using 84 $F_o > 4\sigma(F_o)$ (7 refined parameters). Attempts to refine the oxygen atom at 12*h* anisotropically led to unreasonable values due to high correlations between the coordinates and displacement parameters. Note that the site symmetries for the two cation sites require that they have isotropic atomic displacement parameters.

Heamanite-(Ce) has a perovskite-related structure and adopts the same structure (Mitchell et al. 2017) as isolueshite, $(Na,La)NbO_3$, and tausonite, $SrTiO_3$ (Fig. 5). The disorder of oxygen position is consistent with the octahedral tilting. In this case, we interpret it to be incoherent, thus preserving the overall cubic symmetry in the same way as isolueshite (Krivovichev et al. 2000) whose structure refinement was reported with the same Wyckoff site choices. The observation of incoherent octahedral tilting in a perovskite-type structure was, to the best of our knowledge, reported for the first time by Iyer and Smith (1967) for $LaTa_3O_9$ and later observed for several other cases. As Krivovichev et al. (2000) pointed out, the splitting of the *x* coordinate of anions in the ideal cubic perovskite structure is normally observed close to the point of phase transition to a lower symmetry, and the structure can be regarded as transitional between the ideal $Pm\overline{3}m$ structure and the one derived from it by the ordered rotation (tilting) of octahedra.

The crystal structure of heamanite-(Ce) is characterized by a relatively large difference in size of the various cations occupying the A site, which is a large site with coordination number 12 in the shape of a cuboctahedron. The ideal K–O, Ce–O and Ca–O bond distances, based on Shannon's ionic radii (Shannon 1976) are 3.04, 2.74 and 2.74 Å, respectively. While Ce/Ca substitution is not expected to introduce strain in the crystal structure, the substitution by the larger K, which according to the chemical analysis makes up more than 25% of the A-site, requires expansion of this site. The resulting interatomic distances (refinement with O at 12*h* site) for the A site are 2.605(4) and 2.939(5) Å, whereas in isolueshite they are 2.552(8) and 2.99(1) Å (Krivovichev et al. 2000). The Ti–O interatomic distance is 1.9707(9) Å, whereas isolueshite has a (Nb,Ti)–O distance of 1.979(2) Å (Krivovichev et al. 2000). We refined the occupancy of the A site in heamanite-(Ce) and obtained a mean atomic number that shows some slight deviation from that calculated based on the chemistry: in detail, the structure refinement gave 30.0(3) epfu, whereas the chemistry yielded 32.7(4) epfu. The occupancy of the B site was not refined, as it is occupied almost completely by Ti. The structural data and interatomic distances are reported in Supplemental Table S2 and in the supplemental crystallographic information file (CIF).

Vibrational spectroscopy

The Raman spectrum of heamanite-(Ce) is displayed in Fig. 6, where it is compared with the Raman spectrum of loparite-(Ce) (Popova et al. 2015), and shows two broad bands at 560 and 787 cm^{-1}, with no bands observed above 1000 cm^{-1}. As thoroughly discussed in Popova et al. (2015) for loparite-(Ce), a peculiar feature showed by the Raman spectrum of heamanite-(Ce) is the significant band broadening. In our case the observed peak broadening could be due to the

chemical disorder at the A site, as suggested for loparite-(Ce), or the compressional stress, which is very likely to play a major role since this mineral was found within a diamond.

Discussion

Occurrence and paragenesis

Heamanite-(Ce) occurs as an inclusion in a diamond from the 5034 kimberlite pipe of the Gahcho Kué mine – a joint venture between the De Beers Group and Mountain Province Diamonds Inc. – in the Northwest Territories (63°26′04″N 109°11′10″W) of Canada. The Gahcho Kué kimberlite cluster comprises four main pipes: 5034, Tesla, Hearne and Tuzo. The 5034 kimberlite pipe has a surface area of ~1.7 ha and has been dated radiometrically by the Rb-Sr method on phlogopite as being Middle Cambrian (542.2 ± 2.6 Ma; Heaman et al. 2003). As the deposit has been estimated to contain 13.8 million tonnes of kimberlite to 300 m below surface with an average grade of 1.64 carats/tonne (Hetman et al. 2004), it is considered highly diamondiferous.

Eight inclusions in total were extracted by mechanical crushing of the host diamond, with six being identified as heamanite-(Ce) and the remaining two as rutile (TiO_2). Given the large number of extracted inclusions, we cannot assess if they represent separate inclusions or if some were connected as part of a single large grain. In addition, X-ray diffraction indicated the presence of a calcite grain in contact with the heamanite-(Ce) crystal investigated (Fig. 4). This can be explained by the presence of a carbonated alkaline-rich fluid/melt as the medium for diamond formation, which often involves the simultaneous precipitation of silicates/oxides and carbonates (Kopylova et al. 2010).

The heamanite-(Ce) crystals and the associated rutile were included in a single diamond originating from beneath the southern section of the Slave Craton. In the absence of inclusions suitable for geothermobarometric estimates, the exact depth of origin of the heamanite-(Ce)-bearing diamond cannot be constrained but it is assumed to have originated within the deep lithospheric mantle based on Fourier transform infrared (FTIR) measurements, which provided an average N content (N_{tot}) of 330 atomic ppm and an intermediate nitrogen aggregation state of 41 %B (%B = $100N_B / [N_A + N_B]$, with N_A and N_B being the amount of nitrogen in moderately and fully aggregated nitrogen A- and B-centers, respectively), (Siva-Jothy 2020). These values indicate that the diamond is lithospheric and allow its classification as Type-IaAB (Stachel and Harris 2009).

The presence of rutile and calcite as part of the inclusion assemblage suggests a likely eclogitic origin for the heamanite-(Ce)-bearing diamond. Rutile has previously been described in a number of diamonds in association with eclogitic garnet and omphacitic clinopyroxene (e.g., Deines and Harris 2004; Stachel et al. 2018) and calcite was observed by Sobolev et al. (2009) together with phlogopite and sulphide inclusions in presumed-eclogitic diamonds from Yakutia.

Relationship to other species

Heamanite-(Ce), $(K_{0.5}Ce_{0.5})TiO_3$, can be compared to its Na-analog, loparite-(Ce), $(NaCe)Ti_2O_6$, and to the other natural cubic or pseudo-cubic perovskites with alkali-metals and Ti or Nb: tausonite, $SrTiO_3$, isolueshite, $(Na,La)NbO_3$, goldschmidtite, $(K,REE,Sr)(Nb,Cr)O_3$, and lueshite, $NaNbO_3$. All these phases belong to the perovskite group with the general formula ABO_3 (Mitchell et al. 2017).

Tausonite, isolueshite and goldschmidtite have the same space group as heamanite-(Ce). However, tausonite (Mitchell et al. 2000b) and isolueshite (Krivovichev et al. 2000; Zaitsev et al.

2017) have slightly smaller unit-cell volumes, whereas goldschmidtite (Meyer et al. 2019) has a larger unit-cell volume. As one would expect among structural analogs, the positions of their main diffraction peaks are very similar, in particular the main peak is located at 2.76 Å for all of them except goldschmidtite (located at 2.82 Å), whereas their intensities are different (see Supplemental Table S1).

In contrast, the chemical composition of loparite-(Ce) may vary from one deposit to another (Mitchell et al. 2000a). As a consequence, several structural models have been reported that differ in the degree of distortion of the octahedral framework and the schemes of cation ordering. This might be due to the difficulty in measuring such small grains. There have been several reports of the symmetry of loparite-(Ce) assigning it to cubic, orthorhombic, tetragonal and trigonal systems (see Popova et al. 2017 for an exhaustive review). In terms of diffraction peaks, their positions and intensities are similar to those of heamanite-(Ce). Thus, the most reliable way to distinguish between heamanite-(Ce) and loparite-(Ce) is the chemical composition.

Lueshite is orthorhombic and has a much larger unit-cell volume and very different diffraction peak-positions than heamanite-(Ce) (Mitchell et al. 2014); these two minerals can therefore be distinguished without ambiguity both by composition and structure.

Implications

Although perovskite is common in kimberlites (Chakhmouradian et al. 2000), it is very rare as an inclusion in diamonds. Kopylova et al. (1997a) reported K-REE-Cr-rich tausonite (referred to as strontian K-Cr loparite by these authors) as an inclusion in a diamond from the River Ranch kimberlite (Zimbabwe) and suggested it had formed during a K-metasomatic event that overprinted the chemistry of the ambient mantle. They also suggested it might be linked to

other alkali titanates (i.e., crichtonite-armalcolite, rutile, ilmenite, hawthorneite-yimengite) developed in metasomatic rocks erupted by kimberlites from 70–150 km depths (Kopylova et al. 1997b). Meyer et al. (2019) reported goldschmidtite as an inclusion in a diamond from Koffiefontein (South Africa) and suggested its formation due to extreme metasomatic conditions in the lithosphere that caused exceptional concentrations of Nb, K and LREE. These authors also estimated the formation of the diamond host of goldschmidtite to be about 170 km beneath Earth's surface, at temperatures of about 1200 ºC.

Ryabchikov et al. (1982) suggested that metasomatism in the mantle would be K-rich at greater depths and Na-rich at shallower depths. This suggestion is nominally supported by formation of phlogopite in peridotites at deeper levels and edenite at shallower levels (Winterburn et al. 1990). The formation of K-REE-Cr-rich tausonite (Kopylova et al. 1997), goldschmidtite (Meyer et al. 2019) and heamanite-(Ce) in diamonds further endorses this suggestion of a change in the geochemical character of mantle metasomatism with depth. Discoveries of exotic K and Na-rich metasomatic phases have also been increasing in mantle-derived mantle xenoliths. For instance, priderite, freudenbergite and jeppeite have been observed in a range of metasomatized mantle material (e.g., Haggerty et al. 1994; Giuliani et al. 2012), while the Na-rich analogue of jeppeite, nixonite, was recently discovered (Anzolini et al. 2019), also co-existing with priderite and freudenbergite, in a reaction rim around rutile (Harris et al. 2018). This reaction relationship with rutile raises the possibility that the heamanite-(Ce) may have formed due to a reaction between a pre-existing rutile grain (several are present in the same diamond) and a K-Ce enriched metasomatic fluid similar to that which may have resulted in the formation of the goldschmidtite reported by Meyer et al. (2019). The presence of calcite, if it is contemporaneous and syngenetic with the other inclusions, would support this scenario.

However, in detail, the depth-relationship between K- and Na-rich metasomatism is unclear as fluids within fibrous diamonds can be extremely Na-rich as well as K-rich (e.g., Weiss et al. 2015) and studies of fluids metasomatizing shallower mantle produce a range of K- and Na-rich phases including K-Na-Ca carbonates, kalsilite, phlogopite, K-Na titanates, and phosphates, and alkali sulfates at depths as shallow as ~100 km (Giuliani et al. 2012). It seems clear from this that metasomatic fluids such as the alkali carbonate melts discussed by Giuliani et al. (2012) could be effective metasomatic agents throughout the lower to mid-levels of the continental lithospheric mantle. The exact nature of the phases produced, such as nixonite, jeppeite, heamanite-(Ce) or goldschmidtite may depend also on the nature of precursor Ti-rich phases, that either form reactive substrates (in the case of nixonite – Anzolini et al. 2019) or supply Ti to the fluid through dissolution.

Perovskite reported in a diamond from the Sytykanskaya kimberlite (Siberia) by Hamilton et al. (2003) was dated by the U-Pb method and found to have formed close to the eruption age of the host kimberlite. It is thus possible that the heamanite-(Ce) found at Gahcho Kué is related to this type of syn-kimberlite metasomatic activity and this will have to be confirmed by future geochronology studies, if more crystals are found.

As already discussed for goldschmidtite (Meyer et al. 2019), the precipitation of a phase with such high concentrations of LILE (K, Sr, Ba), LREE, and incompatible HFSE (Ti, Nb) requires an extremely fractionated metasomatic fluid much more enriched in incompatible elements than has been observed for "normal" mantle metasomatism (Bailey 1982; Hofmann 1988; Nielson and Wilshire 1993; Allè re et al. 1995). Meyer et al. (2019) suggested that this enrichment could be achieved during extreme levels of fractionation, where only minuscule amounts remain of an initially much larger volume of metasomatic melt or fluid.

Moreover, the high concentration of radiogenic elements in heamanite-(Ce) may allow for future isotopic dating studies in the systems: Rb-Sr, Sm-Nd, U-Pb, and perhaps even Lu-Hf. Such studies might help to reveal the metasomatic history that led to the formation of heamanite-(Ce) and the fluid-processes that affect the deep roots of continents during diamond formation.

Acknowledgments

C.A. thanks Marta Morana for assistance during the X-ray data collection and Luca Peruzzo for help with the Vickers microhardness test. De Beers Group is thanked for donating the diamond specimen from its Gahcho Kué mine. We thank three anonymous reviewers for suggestions that led to the improvement of the manuscript, and Jennifer Kung for careful editorial handling.

Funding

This research was financially supported by a Canada Excellence Research Chair (CERC) grant to D.G.P., a Natural Sciences and Engineering Research Council Discovery Grant to T.S., and by the Diamond Exploration and Research Training School (DERTS), all funded by NSERC. M.A. acknowledges support from the Italian Ministry for Research and University–Scientific Independence of Young Researchers (MIUR-SIR) MILE DEEp project (grant RBSI140351) and the ERC-StG 2016 TRUE DEPTHS (grant 714936).

References cited

Allègre, C.J., Poirier, J., Humler, E., and Hofmann, A.W. (1995) The chemical composition of the Earth. Earth and Planetary Science Letters, 134, 515–526.

Anzolini, C., Angel, R.J., Merlini, M., Derzsi, M., Tokár, K., M lani, S., Krebs, M.Y., Brenker, F.E., Nestola, F., and Harris, J.W. (2016) Depth of formation of $CaSiO_3$-walstromite included in super-deep diamonds. Lithos, 265, 138–147.

Anzolini, C., Wang, F., Harris, G.A., Locock, A.J., Zhang, D., Nestola, F., Peruzzo, L., Jacobsen, S.D., and Pearson, D.G. (2019) Nixonite, $Na_2Ti_6O_{13}$, a new mineral from a metasomatized mantle garnet pyroxenite from the western Rae Craton, Darby kimberlite field, Canada. American Mineralogist, 104, 1336–1344.

Bailey, D.K. (1982) Mantle metasomatism – continuing chemical change within the Earth. Nature, 296, 525–530.

Bosi, F., Hatert, F., Hålenius, U., Pasero, M., Miyawaki, R., and Mills, S.J. (2019) On the application of the IMA−CNMNC dominant-valency rule to complex mineral compositions. Mineralogical Magazine, 83, 627–632.

Brenker, F.E., Stachel, T., and Harris, J.W. (2002) Exhumation of lower mantle inclusions in diamond: ATEM investigation of retrograde phase transitions, reactions and exsolution. Earth and Planetary Science Letters, 198, 1–9.

Brenker, F.E., Nestola, F., Brenker, L., Peruzzo, L., and Harris, J.W. (2021) Origin, properties, and structure of breyite: The second most abundant mineral inclusion in super-deep diamonds. American Mineralogist, 106, 38–43.

Chakhmouradian, A.R., and Mitchell, R.H. (2000) Occurrence, alteration patterns and compositional variation of perovskite in kimberlites. Canadian Mineralogist, 38, 975–994.

Deines, P., and Harris, J.W. (2004) New insights into the occurrence of ^{13}C-depleted carbon in the mantle from two closely associated kimberlites: Letlhakane and Orapa, Botswana. Lithos, 77, 125–142.

Deines, P., Harris, J.W., and Gurney, J.J. (1991) The carbon isotopic composition and nitrogen content of lithospheric and asthenospheric diamonds from the Jagersfontein and Koffiefontein kimberlite, South Africa. Geochimica et Cosmochimica Acta, 55, 2615–2625.

Donovan, J.J., Kremser, D., Fournelle, J.H., and Goemann, K. (2015) Probe for EPMA: Acquisition, automation and analysis, version 11: Eugene, Oregon, Probe Software, Inc. http://www.probesoftware.com.

Farrugia L.J. (2012) WinGX – Version 2018.3. Journal of Applied Crystallography, 45, 849–854.

Giuliani, A., Kamenetsky, V.S., Phillips, D., Kendrick, M.A., Wyatt, B.A., and Goemann, K. (2012) Nature of alkali-carbonate fluids in the sub-continental lithospheric mantle. Geology, 40, 967–970.

Haggerty, S.E., Fung, A.T., and Burt, D.M. (1994) Apatite, phosphorus and titanium in eclogitic garnet from the upper mantle. Geophysical Research Letters, 21, 1699–1702.

Hamilton, M.A., Sobolev, N.V., Stern, R.A., Pearson, D.G. (2003) SHRIMP U-Pb dating of a perovskite inclusion in diamond: evidence for a syneruption age for diamond formation, Sytykanskaya kimberlite pipe, Yakutia region, Siberia. 8th International Kimberlite Conference: Extended Abstracts, Vol. 8, 3245.

Harris, G.A., Pearson, D.G., Liu, J., Hardman, M.F., Snyder, D.B., and Kelsch, D. (2018) Mantle composition, age and geotherm beneath the Darby kimberlite field, west central Rae Craton. Mineralogy and Petrology, 112, 57–70.

Harte, B., and Hudson, N.F. (2013) Mineral associations in diamonds from the lowermost upper mantle and uppermost lower mantle. In D.G. Pearson, H.S. Grütter, J.W. Harris, B.A. Kjarsgaard, H. O'Brien, N.V. Chalapathi Rao, and S. Sparks, Eds., Proceedings of 10th International Kimberlite Conference, p. 235–253. Springer, New Delhi.

Harte, B., Harris, J.W., Hutchison, M.T., Watt, G.R., and Wilding, M.C. (1999) Lower mantle mineral associations in diamonds from São Luiz, Brazil. In Y. Fei, C.M. Bertka, and B.O. Mysen, Eds., Mantle Petrology: Field Observations and High-Pressure Experimentation: A Tribute to Francis R. (Joe) Boyd, p. 125–153. Geochemical Society Special Publication.

Heaman, L.M. (1997) Global mafic magmatism at 2.45 Ga: Remnants of an ancient large igneous province?. Geology, 25, 299–302.

Heaman, L.M., and Kjarsgaard, B.A. (2000) Timing of eastern North American kimberlite magmatism: continental extension of the Great Meteor hotspot track?. Earth and Planetary Science Letters, 178, 253–268.

Heaman, L.M., Kjarsgaard, B.A., and Creaser, R.A. (2003) The timing of kimberlite magmatism and implications for diamond exploration: a global perspective. Lithos, 71, 153–184.

Hetman, C.M., Smith, B.S., Paul, J.L., and Winter, F. (2004) Geology of the Gahcho Kué kimberlite pipes, NWT, Canada: root to diatreme magmatic transition zones. Lithos, 76, 51–74.

Hofmann, A.W. (1988) Chemical differentiation of the Earth: the relationship between mantle, continental crust, and oceanic crust. Earth and Planetary Science Letters, 90, 297–314.

Holland, T.J.B., and Redfern, S.A.T. (1997) Unit cell refinement from powder diffraction data: the use of regression diagnostics. Mineralogical Magazine, 61, 65–77.

Iyer, P.N., and Smith, A.J. (1967) Double oxides containing niobium, tantalum, or protactinium. III. Systems involving the rare earths. Acta Crystallographica, 23, 740–746.

Kiseeva, E.S., Wood, B.J., Ghosh, S., and Stachel, T. (2016) The pyroxenite-diamond connection. Geochemical Perspectives Letters, 2, 1–9.

Kopylova, M.G., Gurney, J.J., and Daniels, L.R.M. (1997a) Mineral inclusions in diamonds from the River Ranch kimberlite, Zimbabwe. Contributions to Mineralogy and Petrology, 129, 366–384.

Kopylova, M.G., Rickard, R.S., Kleyenstueber, A., Taylor, W.R., Gurney, J.J., and Daniels, L.R. M. (1997b) First occurrence of strontian K-Cr-loparite and Cr-chevkinite in diamonds. Geologiya i Geofizika, 38, 382–397.

Kopylova, M., Navon, O., Dubrovinsky, L., and Khachatryan, G. (2010) Carbonatitic mineralogy of natural diamond-forming fluids. Earth and Planetary Science Letters, 291, 126–137.

Krivovichev, S.V., Chakhmouradian, A.R., Mitchell, R.H., Filatov, S.K., and Chukanov, N.V. (2000) Crystal structure of isolueshite and its synthetic compositional analogue. European Journal of Mineralogy, 12, 597–607.

Levinson, A. (1966) A system of nomenclature for rare-earth minerals. American Mineralogist, 51, 152–158.

455 Locock, A.J., and Mitchell, R.H. (2018) Perovskite classification: An Excel spreadsheet to
456 determine and depict end-member proportions for the perovskite- and vapnikite-
457 subgroups of the perovskite supergroup. Computers & Geosciences, 113, 106–114.

458 Mandarino, J.A. (1976). The Gladstone-Dale relationship; Part I, Derivation of new constants.
459 Canadian Mineralogist, 14, 498–502.

460 McCammon, C. (2001) Deep diamond mysteries. Science, 293, 813–814.

461 Meyer, N.A., Wenz, M.D., Walsh, J.P., Jacobsen, S.D., Locock, A.J., and Harris, J.W. (2019)
462 Goldschmidtite, (K,REE,Sr)(Nb,Cr)O_3: A new perovskite supergroup mineral found in
463 diamond from Koffiefontein, South Africa. American Mineralogist, 104, 1345–1350.

464 Mitchell R.H., Burns P.C., and Chakhmouradian A.R. (2000a) The crystal structures of loparite-
465 (Ce). Canadian Mineralogist, 38, 145–152.

466 Mitchell, R.H., Chakhmouradian, A.R., and Woodward, P.M. (2000b) Crystal chemistry of
467 perovskite-type compounds in the tausonite-loparite series, ($Sr_{1-2x}Na_xLa_x$)TiO_3. Physics
468 and Chemistry of Minerals, 27, 583–589.

469 Mitchell, R.H., Burns, P.C., Knight, K.S., Howard, C.J., and Chakhmouradian, A.R. (2014)
470 Observations on the crystal structures of lueshite. Physics and Chemistry of Minerals, 41,
471 393–401.

472 Mitchell, R.H., Welch, M.D., and Chakhmouradian, A.R. (2017) Nomenclature of the perovskite
473 supergroup: A hierarchical system of classification based on crystal structure and
474 composition. Mineralogical Magazine, 81, 411–461.

475 Momma, K., and Izumi, F. (2011) VESTA 3 for three-dimensional visualization of crystal,
476 volumetric and morphology data. Journal of Applied Crystallography, 44, 1272–1276.

Moore, R.O., and Gurney, J.J. (1985) Pyroxene solid solution in garnets included in diamond. Nature, 318, 553–555.

Nestola, F., Burnham, A.D., Peruzzo, L., Tauro, L., Alvaro, M., Walter, M.J., Gunter, M., Anzolini, C., and Kohn, S.C. (2016) Tetragonal Almandine-Pyrope Phase, TAPP: finally a name for it, the new mineral jeffbenite. Mineralogical Magazine, 80, 1219–1232.

Nestola, F., Korolev, N., Kopylova, M., Rotiroti, N., Pearson, D.G., Pamato, M.G., Alvaro, M., Peruzzo, L., Gurney, J.J., Moore, A.E., and Davidson, J. (2018) $CaSiO_3$ perovskite in diamond indicates the recycling of oceanic crust into the lower mantle. Nature, 555, 237–241.

Nielson, J.E., and Wilshire, H.G. (1993) Magma transport and metasomatism in the mantle: a critical review of current geochemical models. American Mineralogist, 78, 1117–1134.

Pearson, D.G., Brenker, F.E., Nestola, F., McNeill, J., Nasdala, L., Hutchison, M.T., Matveev, S., Mather, K.A., Silversmit, G., Schmitz, S., and others (2014) Hydrous mantle transition zone indicated by ringwoodite included within diamond. Nature, 507, 221–224.

Petříček, V., Dušek, M., and Palatinus, L. (2014) Crystallographic computing system JANA2006: general features. Zeitschrift für Kristallographie, 229, 345–352.

Popova, E.A., Yakovenchuk, V.N., Lushnikov, S.G., and Krivovichev, S.V. (2015) Structural phase transitions in loparite-(Ce): evidences from Raman light scattering. Journal of Raman Spectroscopy, 46, 161–166.

Popova, E.A., Lushnikov, S.G., Yakovenchuk, V.N., and Krivovichev, S.V. (2017) The crystal structure of loparite: a new acentric variety. Mineralogy and Petrology, 111, 827–832.

Ryabchikov, I.D., Schreyer, W., and Abraham, K. (1982) Compositions of aqueous fluids in equilibrium with pyroxenes and olivines at mantle pressures and temperatures. Contributions to Mineralogy and Petrology, 79, 80–84.

Scott Smith, B.H., Danchin, R.V., Harris, J.W., and Stracke, K.J. (1984) Kimberlites near Orroroo, South Australia. In J. Kornprobst, Ed., Kimberlites I: Kimberlites and related rocks, p. 121–142. Elsevier, Amsterdam.

Shannon, R.D. (1976) Revised effective ionic radii and systematic studies of interatomic distances in halides and chalcogenides. Acta Crystallographica, A32, 751–767.

Sheldrick, G.M. (2015) Crystal structure refinement with SHELXL. Acta Crystallographica, C71, 3–8.

Siva-Jothy, W. (2020) Studies of inclusions and their host diamonds from the Gahcho Kué Mine, 148 p. M.Sc. thesis, University of Alberta, Canada.

Smith, E.M., Shirey, S.B., Nestola, F., Bullock, E.S., Wang, J., Richardson, S.H., and Wang, W. (2016) Large gem diamonds from metallic liquid in Earth's deep mantle. Science, 354, 1403–1405.

Smith, E.M., Shirey, S.B., Richardson, S.H., Nestola, F., Bullock, E.S., Wang, J., and Wang, W. (2018) Blue boron-bearing diamonds from Earth's lower mantle. Nature, 560, 84–87.

Sobolev, N.V., Logvinova, A.M., and Efimova, E.S. (2009) Syngenetic phlogopite inclusions in kimberlite-hosted diamonds: implications for role of volatiles in diamond formation. Russian Geology and Geophysics, 50, 1234–1248.

Stachel, T., and Harris, J.W. (2008) The origin of cratonic diamonds–constraints from mineral inclusions. Ore Geology Reviews, 34, 5–32.

Stachel, T., and Harris, J.W. (2009) Formation of diamond in the Earth's mantle. Journal of Physics: Condensed Matter, 21, 364206.

Stachel, T., Harris, J.W., Brey, G.P., and Joswig, W. (2000) Kankan diamonds (Guinea) II: lower mantle inclusion parageneses. Contributions to Mineralogy and Petrology, 140, 16–27.

Stachel, T., Harris, J.W., Hunt, L., Muehlenbachs, K., Kobussen, A., EIMF (2018) Argyle diamonds – how subduction along the Kimberley Craton edge generated the world's biggest diamond deposit. Society of Economic Geologists Special Publication, 20, 145–167. DOI: http://dx.doi.org/ 10.5382/SP.20.06.

Tschauner, O., Ma, C., Beckett, J.R., Prescher, C., Prakapenka, V.B., and Rossman, G.R. (2014) Discovery of bridgmanite, the most abundant mineral in Earth, in a shocked meteorite. Science, 346, 1100–1102.

Tschauner, O., Huang, S., Greenberg, E., Prakapenka, V.B., Ma, C., Rossman, G.R., Shen, A.H., Zhang, D., Newville, M., Lanzirotti, A., and others (2018) Ice-VII inclusions in diamonds: Evidence for aqueous fluid in Earth's deep mantle. Science, 359, 1136–1139.

Weiss, Y., McNeill, J., Pearson, D.G., Nowell, G.M., and Ottley, C.J. (2015) Highly saline fluids from a subducting slab as the source for fluid-rich diamonds. Nature, 524, 339–342.

Winterburn, P.A., Harte, B., and Gurney, J.J. (1990) Peridotite xenoliths from the Jagersfontein kimberlite pipe: I. Primary and primary-metasomatic mineralogy. Geochimica et Cosmochimica Acta, 54, 329–341.

Zaitsev, A.N., Zhitova, E.S., Spratt, J., Zolotarev, A.A., and Krivovichev, S.V. (2017) Isolueshite, $NaNbO_3$, from the Kovdor carbonatite, Kola peninsula, Russia: composition,

crystal structure and possible formation scenarios. Neues Jahrbuch für Mineralogie-Abhandlungen, 194, 165–173.

Figure captions

Figure 1. Optical image showing the diamond that contained heamanite-(Ce) associated with rutile (before breakage).

Figure 2. a-f) Backscattered images of the six polished heamanite-(Ce) crystals extracted from their diamond host. Red dots indicate where EPMA measurements were collected.

Figure 3. The composition of heamanite-(Ce) plotted on the tausonite – perovskite – loparite & heamanite, and $[(Na,K)NbO_3] – [(Ca,Sr,Ba,Pb)TiO_3] – [(Na,K)_{0.5}REE_{0.5}TiO_3]$, ternary diagrams (modified after Locock and Mitchell 2018).

Figure 4. The crystal of heamanite-(Ce) analyzed both by micro-Raman spectroscopy and single-crystal X-ray diffraction attached to a glass fiber. Crystal shape has been affected by polishing.

Figure 5. Clinographic projection of the crystal structure of heamanite-(Ce) (one unit cell) with splitting of the O site to the 12*h* site with ¼ occupancy. The A site is displayed in yellow, and the B site is in blue.

Figure 6. Uncorrected Raman spectrum of heamanite-(Ce) (black curve) using a 532 nm excitation laser, compared to loparite-(Ce) (blue curve; Popova et al. 2015). Spectra are offset for clarity. Both spectra are overwhelmed by fluorescence below ~300 wavenumbers.

563 **Table 1:** EPMA-WDS analyses (wt%) for heamanite-(Ce) (n = 34). Fe given as Fe_2O_3 (total) by
564 analogy with loparite-(Ce) (Mitchell et al. 2000a).
565

Constituent	Mean	Range	Stand. Dev. (σ)	Reference Material
CaO	10.70	10.39–10.92	0.10	$CaSiO_3$ wollastonite NY
K_2O	7.38	7.28–7.49	0.05	$KAlSi_3O_8$ sanidine Itrongay
Na_2O	0.16	0.09–0.54	0.08	$NaAlSi_3O_8$ albite VA 131705
Ce_2O_3	13.77	13.57–14.02	0.09	$CePO_4$
La_2O_3	8.22	8.07–8.37	0.08	$LaPO_4$
Pr_2O_3	0.84	0.77–0.90	0.03	$PrPO_4$
Nd_2O_3	1.59	1.52–1.65	0.03	$NdPO_4$
SrO	6.69	6.51–6.85	0.10	$SrTiO_3$
BaO	2.96	2.89–3.03	0.03	$BaSi_2O_5$ sanbornite, Fresno
ThO_2	0.36	0.29–0.43	0.04	Thorianite
PbO	0.15	0.12–0.19	0.02	$PbSiO_3$ alamosite glass
TiO_2	45.77	45.17–46.18	0.21	TiO_2 rutile MTI
Cr_2O_3	0.32	0.30–0.35	0.01	Cr_2O_3 chromium oxide Alfa
Al_2O_3	0.10	0.08–0.15	0.01	Frank Smith pyrope garnet
Fe_2O_3	0.09	0.08–0.10	0.01	Fe_2SiO_4 fayalite Rockport
Nb_2O_5	0.87	0.80–0.97	0.04	Niobium, Nb ESPI
UO_3	0.01	0.00–0.06	0.02	Uraninite UO_2
Total	99.98	99.29–100.51	0.29	

Note: Data have been rounded to the nearest 0.01 wt% oxide.
566

567 **Table 2:** List of *d*-spacings (in Å), re ative intensities and *hkl* indices for heamanite-(Ce),
568 calculated from the single-crystal X-ray diffraction measurements.
569

I_{obs} (%)	d_{obs} (Å)	I_{calc} (%)	d_{calc} (Å)	*h*	*k*	*l*
100	**2.764**	**100**	**2.767**	**1**	**1**	**0**
7	2.259	7	2.259	1	1	1
31	**1.954**	**41**	**1.956**	**2**	**0**	**0**
42	**1.596**	**36**	**1.597**	**2**	**1**	**1**
20	**1.382**	**10**	**1.383**	**2**	**2**	**0**
15	**1.236**	**13**	**1.237**	**3**	**1**	**0**
6	1.183	2	1.180	3	1	1
8	1.128	6	1.130	2	2	2
19	**1.045**	**16**	**1.046**	**3**	**2**	**1**
2	0.977	3	0.978	4	0	0
7	0.921	7	0.922	4	1	1

Figure 1

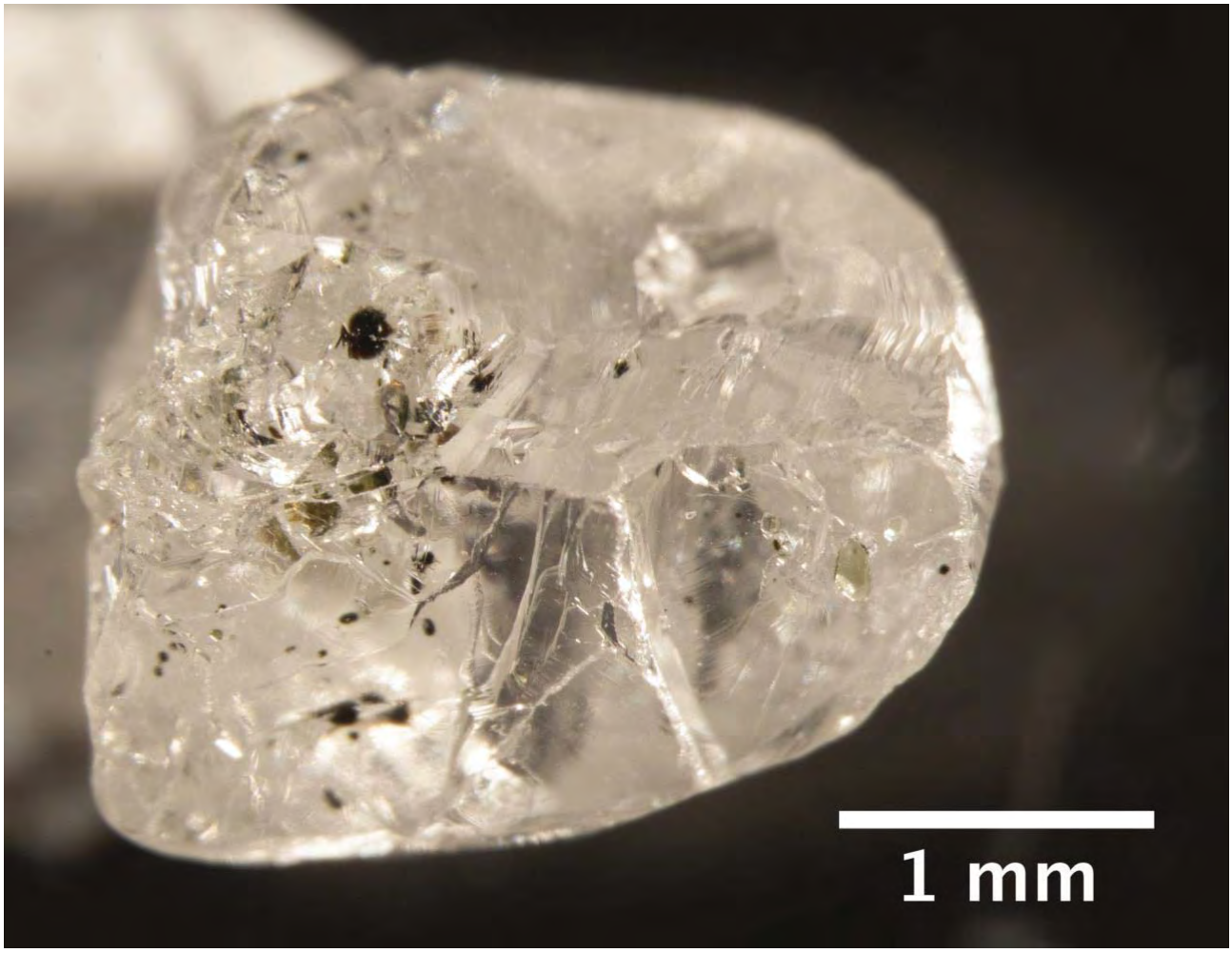

Figure 2

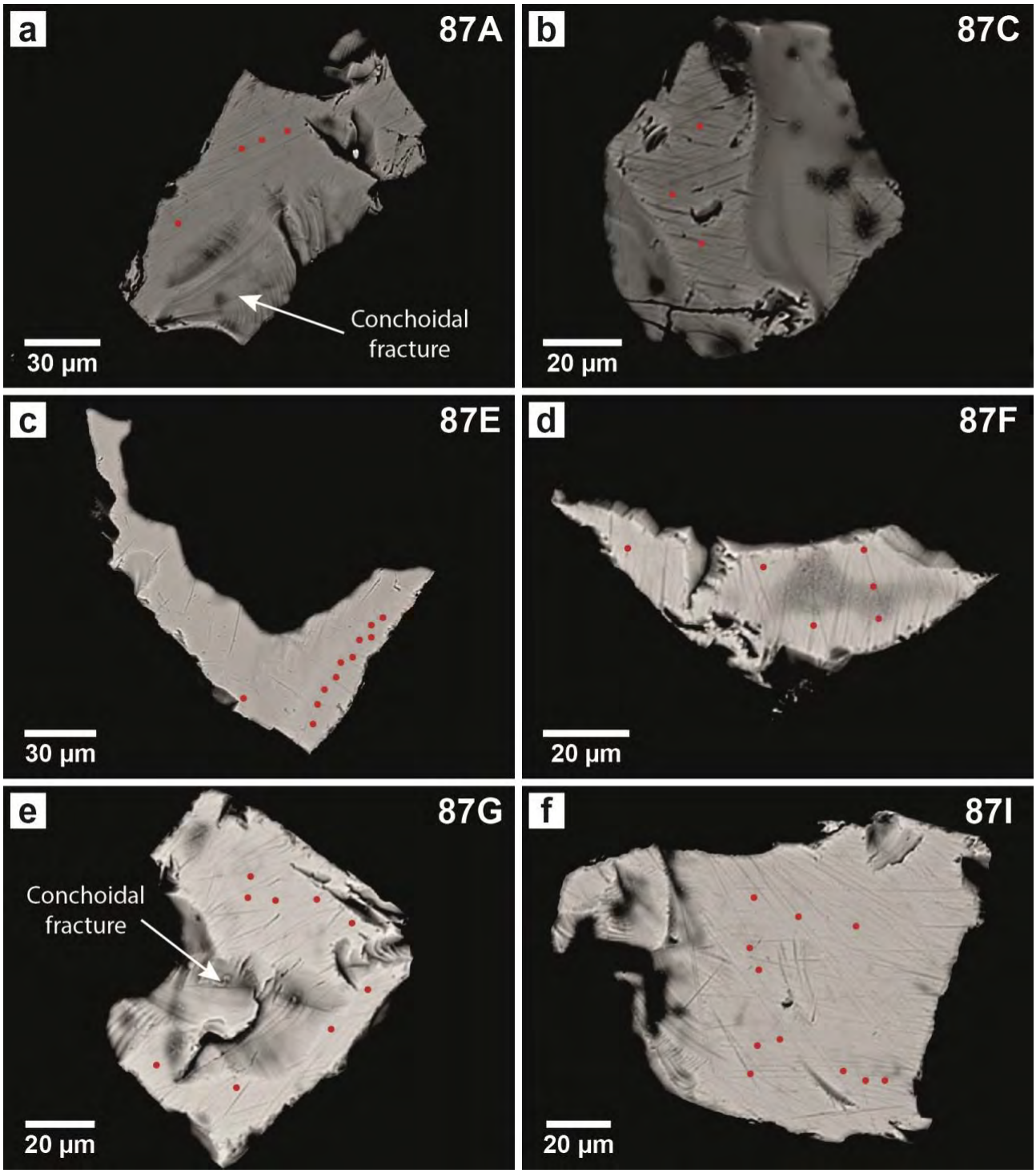

This is the peer-reviewed, final accepted version for American Mineralogist, published by the Mineralogical Society of America.
The published version is subject to change. Cite as Authors (Year) Title. American Mineralogist, in press.
DOI: https://doi.org/10.2138/am-2022-8098. http://www.minsocam.org/

Figure 3

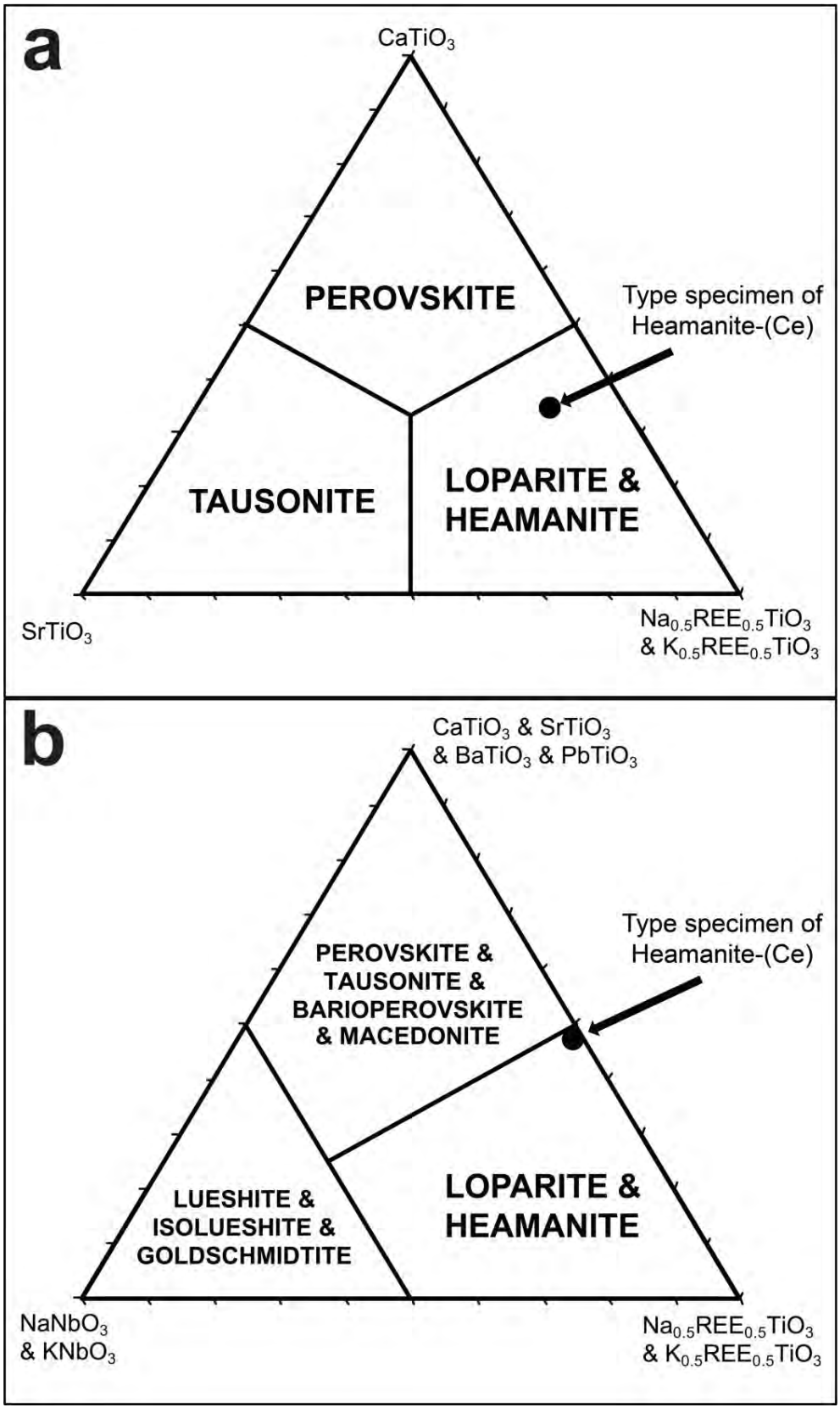

This is the peer-reviewed, final accepted version for American Mineralogist, published by the Mineralogical Society of America.
The published version is subject to change. Cite as Authors (Year) Title. American Mineralogist, in press.
DOI: https://doi.org/10.2138/am-2022-8098. http://www.minsocam.org/

Figure 4

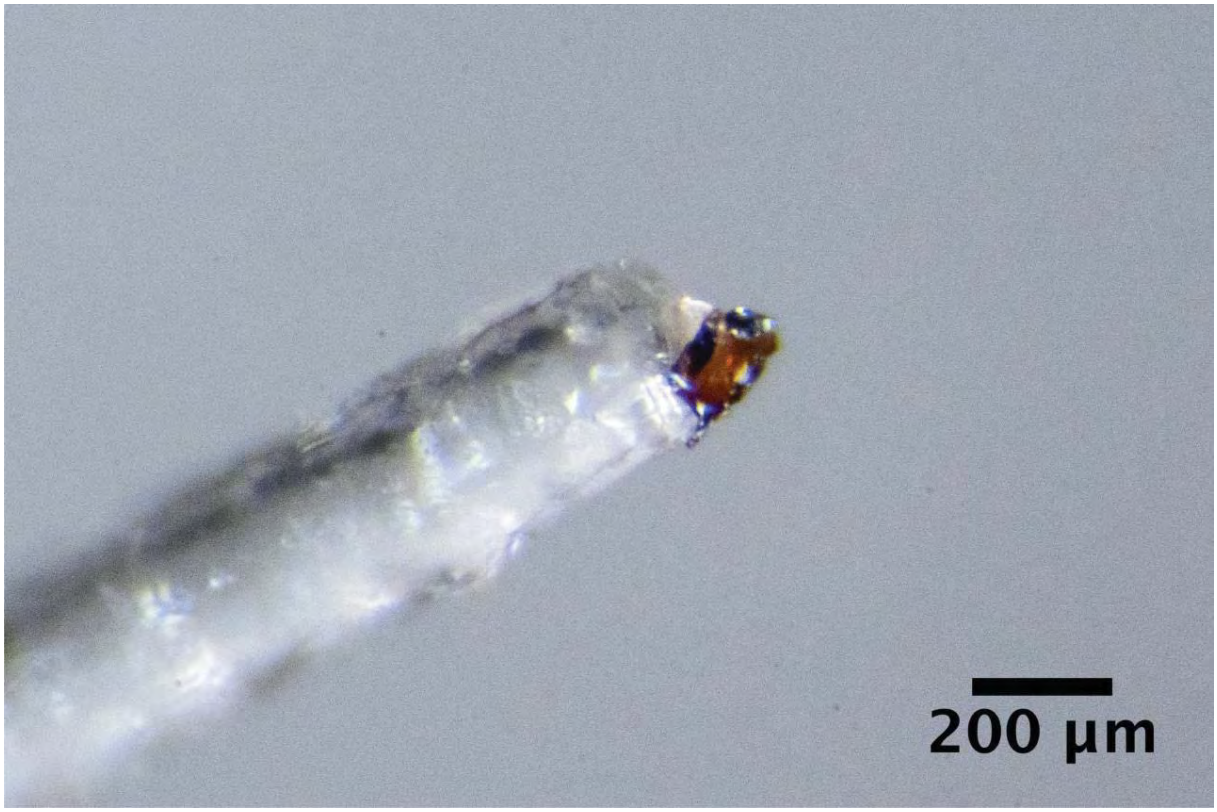

This is the peer-reviewed, final accepted version for American Mineralogist, published by the Mineralogical Society of America.
The published version is subject to change. Cite as Authors (Year) Title. American Mineralogist, in press.
DOI: https://doi.org/10.2138/am-2022-8098. http://www.minsocam.org/

Figure 5

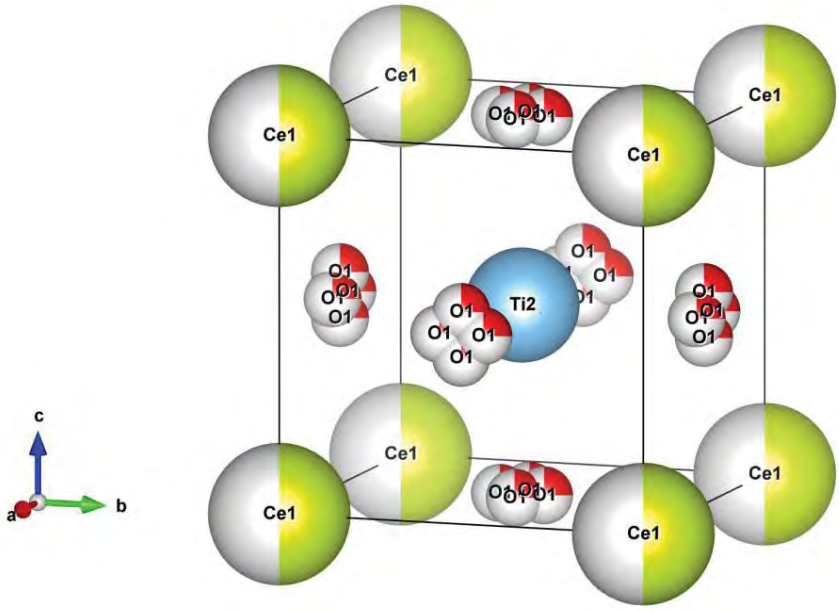

This is the peer-reviewed, final accepted version for American Mineralogist, published by the Mineralogical Society of America.
The published version is subject to change. Cite as Authors (Year) Title. American Mineralogist, in press.
DOI: https://doi.org/10.2138/am-2022-8098. http://www.minsocam.org/

Figure 6